

High-Throughput Electrophoretic Mobility Shift Assays for Quantitative Analysis of Molecular Binding Reactions

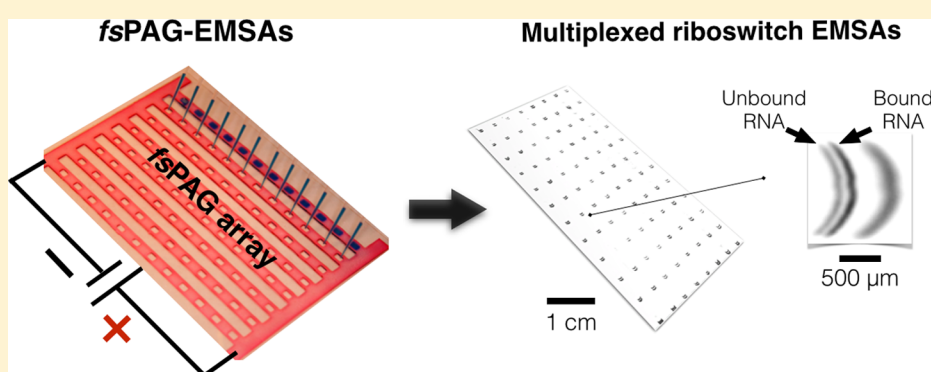
Yuchen Pan,[†] Todd A. Duncombe,[†] Colleen A. Kellenberger,[‡] Ming C. Hammond,^{‡,§} and Amy E. Herr^{*,†}

[†]Graduate Program in Bioengineering, University of California San Francisco and University of California Berkeley, Berkeley, California 94720, United States

[‡]Department of Chemistry, University of California Berkeley, Berkeley, California 94720, United States

[§]Department of Molecular and Cell Biology, University of California Berkeley, Berkeley, California 94720, United States

S Supporting Information



ABSTRACT: We describe a platform for high-throughput electrophoretic mobility shift assays (EMSAs) for identification and characterization of molecular binding reactions. A photopatterned free-standing polyacrylamide gel array comprised of 8 mm-scale polyacrylamide gel strips acts as a chassis for 96 concurrent EMSAs. The high-throughput EMSAs was employed to assess binding of the Vc2 cyclic-di-GMP riboswitch to its ligand. In optimizing the riboswitch EMSAs on the free-standing polyacrylamide gel array, three design considerations were made: minimizing sample injection dispersion, mitigating evaporation from the open free-standing polyacrylamide gel structures during electrophoresis, and controlling unit-to-unit variation across the large-format free-standing polyacrylamide gel array. Optimized electrophoretic mobility shift conditions allowed for 10% difference in mobility shift baseline resolution within 3 min. The powerful 96-plex EMSAs increased the throughput to ~10 data/min, notably more efficient than either conventional slab EMSAs (~0.01 data/min) or even microchannel based microfluidic EMSAs (~0.3 data/min). The free-standing polyacrylamide gel EMSAs yielded reliable quantification of molecular binding and associated mobility shifts for a riboswitch–ligand interaction, thus demonstrating a screening assay platform suitable for riboswitches and potentially a wide range of RNA and other macromolecular targets.

Riboswitches are functional RNA molecules that play a key role in gene regulation of many important processes in diverse bacterial species.¹ Located in the 5' untranslated regions (UTRs) of mRNA, riboswitches directly bind to small molecule metabolites through their aptamer domain, triggering a conformational change that alters expression of the downstream gene.² Owing to selective ligand binding, riboswitches have garnered interest as promising and largely unexplored antibiotic drug targets.³ To maximize the chance of discovering riboswitch-targeting antibacterial ligands, a rapid and robust screening platform is required to efficiently identify potential riboswitch-binding compounds from compound libraries.^{3,4} Gold-standard screening tools include fluorescence polarization (FP)⁵ and fluorescence resonance energy transfer (FRET).⁶ While powerful, FP and FRET are not readily implemented as high-throughput assays, as both are sample-intensive, are slow, and require substantial infrastructure.⁷ Recently, droplet

microfluidic FP and FRET have improved assay throughput but have not been applied to the study of riboswitches.^{8,9}

Alternatively, electrophoretic mobility shift assays (EMSAs), introduced by Garner and Revzin,¹⁰ have played an important role in the study of numerous molecular binding interactions including riboswitches. Widely employed, EMSAs measure changes in the physical properties of a target analyte (i.e., size, charge, conformation) upon binding with a ligand. Binding-induced changes can shift the electrophoretic mobility of the target analyte, a measurable quantity allowing quantitative characterization of the binding reaction.^{11,12} Yet, conventional EMSAs are conducted with slab polyacrylamide gel electrophoresis (PAGE), which is low-throughput and not suitable for

Received: July 21, 2014

Accepted: September 18, 2014

Published: September 18, 2014

screening assays.^{13,14} For example, binding of the Vc2 GEMM-I riboswitch to its ligand cyclic di-GMP (c-di-GMP), an important second messenger in bacteria,¹⁵ induces a significant structural compaction of the riboswitch aptamer.¹⁶ This compaction results in a higher electrophoretic mobility in the gel matrix than its free form. To electrophoretically resolve the bound and unbound RNAs via conventional slab-gel EMSAs requires up to 17 h.¹⁷

Capillary electrophoresis (CE) is an efficient separation modality and Stebbins et al.¹⁸ introduced CE for EMSAs to analyze binding between the trp repressor in *Escherichia coli* and the trp operator (DNA). The mobility shift was resolved in 6 min. To further advance the quantitative capacity and throughput of EMSAs, Karns and colleagues¹⁷ introduced microfluidic PAGE to study the binding characteristics of S-adenosylmethionine-I riboswitches. A key advantage of this microfluidic electrophoresis platform is the efficient heat dissipation due to a large surface area-to-volume ratio in microchannels. This favorable thermal transport characteristic enables the use of high electric field (e.g., 400 V/cm in-chip and ~10 V/cm on slab PAGE), thus resolving binding pairs in 30 s (compared to 17 h on slab PAGE). However, regardless of the rapid analysis, the microchip format was limited to single and serial implementation of separations. As a result, the entire assay protocol (i.e., loading-separation-washing) required ~3 min, limiting usefulness in high-throughput screening. A recent breakthrough in increasing analytical throughput takes advantage of multiplexed formats. In 2000, Ferrance et al.¹⁹ demonstrated an 8-plex multichannel microfluidic separation system for rapid clinical diagnostics. Later, Ross and colleagues²⁰ demonstrated a 16-plex gradient elution moving boundary electrophoresis tool for monitoring enzyme activity and inhibition. Researchers have also introduced microfluidic systems compatible with powerful, conventional biological tools (e.g., a microplate format). For example, a 384-plex radial microfluidic capillary electrophoresis tool developed by Emrich et al.²¹ supported ultrahigh-throughput genetic analyses. In 2003, Gaunt et al.²² established a microplate gel array platform for SNP genotyping, in which a PAG molded with sample wells was seated on a silane-treated glass plate. With the molding strategy, 768 wells were fabricated in the PAG sheet, yielding the highest reported multiplexed electrophoresis tool to our knowledge. At the single-cell level, Gutzkow et al.²³ developed a 96-plex minigel platform for high-throughput comet assays, using cell-suspended agarose droplets patterned on a piece of polyester film (Gel bond). Engelward and colleagues^{24,25} have developed the CometChip, a sheet of agarose gel patterned with microwells that house single cells. The CometChip has been applied to assess genotoxicity mediated by engineered nanoparticles. In 2014, we introduced a microfluidic device that enables completion of thousands of concurrent single-cell western blots.²⁶

Building on our previous work which reported electrophoretic resolution of proteins in 96-plex fsPAG electrophoresis (fsPAGE) assay,²⁷ we now address an unmet throughput need for riboswitch screening. We detail design considerations for successful introduction of multiplexed fsPAG-EMSAs. Screening for changes in riboswitch conformation presents new analytical challenges for an EMSA system. For context, our previous fsPAGE protein analyses measured large relative electrophoretic mobility shifts between adjacent peaks (i.e., 2× changes in the electrophoretic mobility) in a standard low conductivity buffer. Riboswitch mobility shifts are compara-

tively small, 10% relative mobility shifts (bound and unbound), and require high conductivity buffers, which limits the possible assay time before heating effects disrupt the assay. In this work, we quantitatively characterized the fsPAGE platform and optimized the system to improve sample injection and resolving power over short migration distances and assay times. Through optimization studies, we determined optimal conditions for performing high-throughput (<3 min electrophoresis) and massively multiplexed (96-plex) fsPAGE. In the process, we elucidated fundamental physical relationships inherent to the fsPAGE platform, not previously described.²⁷ In addition, this work analyzed how the electrode proximity to EMSA units affected electrophoretic velocity variation across the large 96-plex array. Through optimization, we achieved excellent unit-to-unit uniformity across a 96-plex array, an important advance over previous fsPAGE studies.²⁷ After optimization, we applied the fsPAG-EMSA platform to 96 concurrent EMSAs of the Vc2 riboswitch aptamer binding interaction with c-di-GMP. fsPAG-EMSAs yielded assay throughput of 10 data points per minute, orders of magnitude more efficient than either conventional slab or microfluidic EMSAs. Successful fsPAG-EMSAs may form the basis for large-scale screening of riboswitches and other macromolecular targets.

MATERIALS AND METHODS

Reagents. Solutions of 30% (w/v) (29:1) acrylamide/bis-acrylamide, glacial acetic acid, glycerol, and Triton X-100 were purchased from Sigma-Aldrich (St. Louis, MO). 10× Tris-borate-magnesium–potassium (TBMK) run buffer was prepared by dissolving 890 mM tris base (Fisher Scientific, Hampton, NH), 890 mM boric acid (Fisher Scientific), 30 mM magnesium chloride (EMD chemical, Gibbstown, NJ), and 100 mM potassium chloride (Sigma-Aldrich) into 1 L of molecular biology grade (DNase-, RNase- and Protease-free) water (Mediatech, Manassas, VA). AlexaFluor 488 (AF488) conjugated Trypsin Inhibitor (TI*, 21 kDa), Ovalbumin (OVA*, 45 kDa) were purchased from Life Technologies Corporation (Carlsbad, CA). Photoinitiator 2,2-azobis[2-methyl-N-(2-hydroxyethyl) propionamide] (VA-086) was purchased from Wako Chemical (Richmond, VA). GelBond PAG film was purchased from Lonza (Basel, Switzerland). Photomasks were designed with AutoCad student edition (Autodesk, San Rafael, CA) and printed with a Brother MFC-9320C digital color printer (Brother International Corporation, Bridgewater, NJ) on a transparent film (3M, St. Paul, MN).

Preparation of RNAs. Fluorescent riboswitch RNAs were prepared following previously described protocols.¹⁷ Briefly, DNA templates were generated using primers that appended the T7 promoter sequence directly upstream of the aptamer sequence. RNAs were then transcribed *in vitro* using T7 RNA polymerase (NEB, Ipswich, Massachusetts) and purified by denaturing PAGE following standard protocols. Following oxidation of the 3' ribose with NaIO₄ (Sigma-Aldrich), RNAs were reacted with AlexaFluor 488 hydrazide (Life Technologies) in the dark and purified via denaturing PAGE. The accurate RNA concentration was determined via a thermal hydrolysis assay²⁸ to remove effects of hypochromicity, and the labeling efficiency was calculated as previously described.¹⁷

Protein (TI* and OVA*) solutions were prepared by diluting a stock solution with water and 10× TBMK into indicated concentrations. To prepare the binding reaction solution, c-di-GMP riboswitch, 10× TBMK buffer, 1 mg/mL yeast tRNA (Life Technologies), and water were mixed in a 0.5 mL

Eppendorf Lo-Bind tube at indicated concentrations. The final mixture solution contained 1× TBMK, 100 $\mu\text{g/mL}$ yeast tRNA, and 1 μM c-di-GMP riboswitch. Yeast tRNA is used to improve the stability of RNA against degradation. The mixture was heated at 70 °C for 3 min and cooled for 10 min at room temperature to renature the RNA. c-di-GMP and an internal standard (TI*) were added into the solution. The sample mixture was placed in a dark room and equilibrated at room temperature for 1 h.

fsPAG Fabrication and Electrophoresis Operation. fsPAGs were fabricated via UV photopatterning.²⁷ The PAG precursor solution contained 20% T acrylamide (w/v), 3.3% C bis-acrylamide cross-linker (w/w), and 0.2% VA-086 photoinitiator (w/v). Prior to UV exposure, the precursor solution was degassed for 2–3 min under house vacuum with sonication. To briefly recap the fabrication, a surface-functionalized polymer sheet (Gelbond) was placed on top of a borosilicate glass substrate. Two spacers with predefined thickness (greater than Gelbond) were then aligned on two sides of Gelbond and a glass plate was laid on spacers to act as a top cover. The PAG precursor solution was pipetted into the gap between the Gelbond and the glass cover, such that the height of fsPAG was defined by the height difference between the spacers and the Gelbond (from 70 to 600 μm). The PAG precursor solution was then exposed to UV light through a photomask, selectively polymerizing the regions of interest. The intensity and time for UV exposure were optimized for each monomer concentration. For 20% T 3.3% C PAGs, 70 s exposure at 20 mW/cm^2 (measured by OAI 308 UV intensity meter, OAI, San Jose, CA) was employed. After UV exposure, the polymerized fsPAG structures were gently washed with water to remove unpolymerized monomers. The entire process (mask design, printing, and gel fabrication) takes 1 h, making the process amenable to rapid prototyping of new device designs and gel conditions. fsPAG height was measured with MicroXAM-100 Optical Profilometer (ADE phase Shift, Tucson, AZ).

After photopatterning, the fsPAG was soaked in run buffer for 10 min on an Orbitron shaker. When removed, a pipet tip connected to house vacuum was applied to and around each well to remove residual run buffer via suction. Sample solution was then manually pipetted into the sample wells. Two electrode wicks wetted with run buffer were aligned atop the fsPAG at both ends of the sheet-like structures. Graphite electrodes were placed in contact with the electrode wicks. The entire electrophoresis setup was housed in an environmental chamber²⁷ (see the Supporting Information, Figure S1) and connected to an external high-voltage power supplier (PowerPac HV; Bio-Rad Laboratories). Unlike conventional slab gel electrophoresis, submerging the thin fsPAG structure in buffer confounds the assay in three ways. First, submerging the fsPAG structure makes loading of the <1 μL sample volumes into the injection wells difficult. This is because ultralow volume loading relies on hydrophilicity of the well surface which loses effectiveness when submerging under buffer solution. Second, owing to the placement of the electrode wicks and the use of thin fsPAG features (*z*-axis), submersion leads to loss of analyte, as species readily disperse out of the thin gel and into the covering buffer layer due to diffusion and the *z*-component of the electric field. Mass losses to the buffer layer result in reduced detection sensitivity performance. Lastly, the covering buffer greatly increases the system conductivity, which leads to higher current value and temperature, potentially affecting the

binding affinity. Unless otherwise stated, fsPAGE was performed with 100 μm 20% T 3.3% C fsPAG in 1× TBMK buffer containing 20% glycerol at an applied electric field of 60 V/cm.

Imaging. Fluorescence imaging was conducted using an inverted epi-fluorescence microscope (Olympus IX-70) equipped with a 2× objective (PlanApo, N.A. = 0.08, Olympus, Center Valley, PA). The illumination source was an X-Cite exacte mercury lamp (Lumen Dynamics, Mississauga, Canada) filtered through a XF100-3 filter (Omega Optical, Battleboro, VT). A Peltier cooled charge-coupled device (CCD) camera (CoolSNAP HQ2, Roper Scientific, Trenton, NJ) attached to the microscope collected fluorescence images. Large area imaging for the 96-plex EMSAs was performed with a scan slide function controlled by Metamorph software (Molecular Devices, Sunnyvale, CA). Image processing was performed with ImageJ (NIH, Bethesda, MD) and subsequent data analysis was performed with OriginPro 8.0 (OriginLab, Northampton, MA). Fluorescence intensity profiles were generated by averaging the fluorescence signal over the transverse dimension of fsPAG, and each peak was fitted with a Gaussian distribution. To quantify the fluorescence intensity of the analytes, we took the height of the Gaussian peaks. To quantify the resolving power of electrophoresis, we utilized the metric separation resolution (SR), defined as $\text{SR} = \Delta L / 4\sigma$. ΔL is the distance between bands (scale with migration distance) and σ the standard deviation (bandwidth = 4σ).

Computational Simulations. Simulation of fsPAGE was performed on COMSOL Multiphysics v4.2a (COMSOL, Inc., Palo Alto, CA) with Transport of Diluted Species and Electric Currents 3D physics modules. Developed to assess nonuniformity of electric field lines, our model neglected thermal effects and employed two assumptions. First, evaporation during electrophoresis was neglected and the height of the fsPAG structures was assumed to remain constant. Second, temperature was assumed to remain constant. Run buffer (1× Tris-glycine) conductivity in aqueous solution was measured by a B-173 Compact Conductivity Meter (Horiba Scientific, Kyoto, Japan). Run buffer conductivity in the fsPAG structures was estimated to be similar to that of PAG in glass microfluidic chips, as described by Duncombe et al.²⁹ The mobility and diffusivity of the model protein, TI, was estimated as per Herr and Singh³⁰ and Hughes et al.³¹ The voltage boundary conditions were set at each terminus of the fsPAG structure. For post-simulation data analysis, we averaged the protein concentrations over the transverse fsPAG lane dimension at the 120 s time point to generate analyte concentration profiles, which were then analyzed in OriginPro 8.0 to calculate the band widths. In simulations, electric field strength was set to 60 V/cm.

■ RESULTS AND DISCUSSION

To develop a high-throughput fsPAG-EMSA platform for screening riboswitch-ligand interactions (Figure 1A), we first focused on device and assay optimization, including control of injection dispersion, evaporation from the open gel structures, and the unit-to-unit variation across 96 concurrent separations. We applied the optimized 96-plex EMSA array (Figure 1B) to study binding of the Vc2 c-di-GMP riboswitch to its ligand.

Sample Loading in fsPAGE Structures. Electrophoretic separations in planar microfluidic devices traditionally employ a *t*-channel configuration where sample loading and subsequent separation occur in each of the two orthogonal channels.

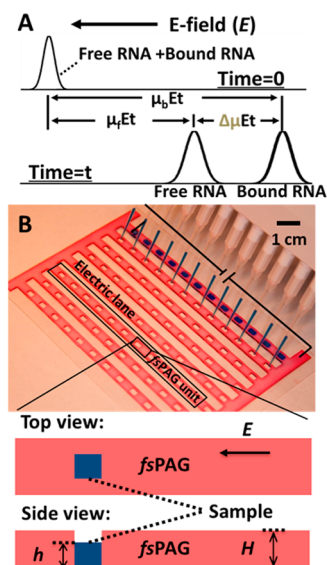


Figure 1. fsPAG design for microfluidic EMSAs. (A) Bound RNA demonstrates an increased mobility relative to unbound RNA due to conformational compaction. Mobilities of the free and bound RNA are represented by μ_f and μ_b . (B) Image of a 96-plex fsPAG array. Sample wells are open rectangular regions. The PAG is dyed red to enhance contrast. A schematic of a single fsPAG unit is shown below. The sample well is embedded in the fsPAG. Gel structure and sample fluid heights are indicated by H and h .

However, in fsPAG, sample loading and injection are performed along a single spatial axis, in a manner similar to conventional slab PAGE (Figure 1B). Therefore, the quality of the electrophoretic separation is sensitive not just to injection dispersion of analyte but also to conditions in the sample well during the separation process. Given the open format and orientation of the fsPAG structures, sample is pipetted into the sample well from above (Figure 2A). Depending on the volume of the sample well and the volume of the sample itself, the sample aliquot may not necessarily fill the entire well volume.

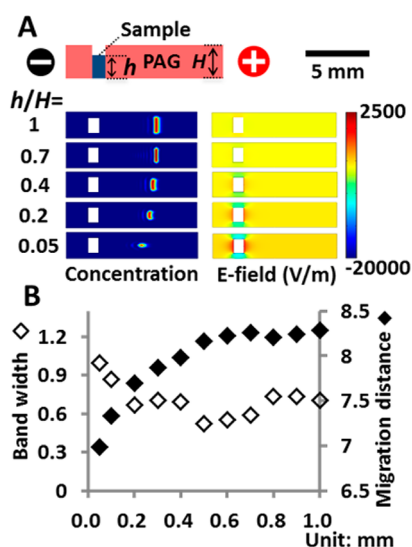


Figure 2. (A) COMSOL simulation of fsPAGE of TI with different sample loading heights. Axial well length = 1 mm, $E = 60$ V/cm. (B) Simulation results of bandwidth and migration distance for different h/H conditions.

Thus, to understand the sensitivity of separation performance on sample loading in this open sample well configuration, we simulated fsPAGE and the associated electric field strengths across a range of sample aliquot heights (h) relative to the fsPAG structure height (H). Though the simulation is performed for TI, the results of band shape and electric field also apply to a wide range of biomolecules including riboswitches. Electrical resistance of the sample well can be described by $R_w = \rho \cdot l_w / (w_w \cdot h)$, where ρ is sample resistivity, and l_w and w_w are the axial length and width of the well. Consequently, reducing h would increase the resistance in the well, causing a greater voltage drop over the sample well region along the separation axis (U_w) and, by Ohm's law, a reduced voltage drop over the gel region along the separation axis (U_g), as $U_w + U_g = U$ (applied voltage). As shown in Figure 2A, when $h/H \geq 0.4$, no notable transverse band skew or associated skew-induced axial dispersion was observed. Appreciable nonuniformities in the electric field distributions were also not evident. In contrast, when $h/H < 0.4$, skewing of the protein peak was observed as is the reduced migration distance. The $h/H < 0.4$ configuration essentially described a poorly filled sample well. Dispersion observed in the poorly filled well cases is attributed to high resistance and correspondingly high voltage drops across the sample well when limited sample volume is present. Protein migration distance (Figure 2B) increased monotonically with increasing fractional fluid height in the well (h/H). Concomitantly, we observed a general trend of decrease in bandwidth with increasing h/H . Consequently, we adopt sample well loading height in the $0.4 < h/H < 1.0$ range as a design rule for fsPAGE.

Thermal Analysis of Open fsPAG Structures. For a given fsPAG structure, we consider Joule heating during electrophoresis. We can describe the heat balance by

$$UI = A(\dot{q}_C + \dot{q}_E) \quad (1)$$

On the left-hand side of eq 1, we see heat generation given by the product of the applied voltage (U) and the electrical current (I). The right-hand side represents heat loss from convection \dot{q}_C and evaporation \dot{q}_E , where A is the fsPAG structure surface area. We can estimate $A = lw$ and $I = U\sigma_g wH/l$, where l is fsPAG structure length, w is the structure width, H is the structure height, and σ_g is fsPAG conductivity. Given the large ratio (50–100) of the planar dimension (~ 1 cm) to the fsPAG height (~ 0.1 mm), we neglect heat dissipation from the sides of the gel structures. We can relate heat losses to operating conditions and the structure geometry:

$$\frac{U^2}{l^2} \sigma_g H = \dot{q}_C + \dot{q}_E \quad (2)$$

Equation 2 states the sum of \dot{q}_C and \dot{q}_E increases with σ_g and H . According to Langmuir's evaporation model and the Antoine equation describing the temperature–vapor pressure relationship,³² both \dot{q}_C and \dot{q}_E increase with temperature. Therefore, increasing either σ_g or H would result in both higher \dot{q}_C and \dot{q}_E . In addition, the relative evaporative loss rate (fractional water loss in the gel body) also increases with H (see the Supporting Information). Dependences on geometry and thermal properties are directly relevant to riboswitch fsPAG-EMSA operation. First, riboswitch binding to ligand depends on the local ions and their concentrations. As such, the TMBK buffer employed for riboswitch EMSAs is appreciably more conductive than typical gel electrophoresis buffers. For context, the TMBK

buffer is ~ 7 times more conductive than tris-glycine buffer systems previously utilized in *fs*PAGE for protein analysis. Second, the open architecture of the *fs*PAG structures is susceptible to evaporative loss, leading to weak electrophoretic stability.

To understand the as-of-yet unexplored influence of device geometry (H) on the thermal and electrical characteristics of *fs*PAG-EMSA, we monitored the relative current (normalized by initial current value) during *fs*PAGE for a range of H values (70–600 μm). For gels where $H < 70 \mu\text{m}$, both fabrication and sample loading were difficult, causing irreproducible initial conditions so these *fs*PAG structures were not considered. For all structures studied, U was held fixed ($E = 60 \text{ V/cm}$) and the TBMK run buffer contained 20% glycerol (glycerol helps to improve current stability and details can be found in a later section). As shown in Figure 3A, taller *fs*PAG structures ($H \geq$

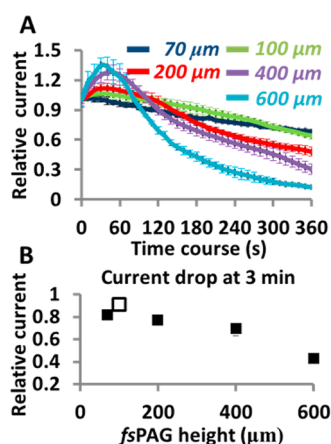


Figure 3. *fs*PAG geometry impacts current stability during electrophoresis. (A) Current stability over time during *fs*PAGE at $E = 60 \text{ V/cm}$. *fs*PAG of 70–100 μm preserves most conductivity. (B) Current drop measurement for a range of *fs*PAG structure heights at 3 min. The highest relative current (white data point) is observed at 100 μm .

400 μm) exhibited an initial ramp up in current followed by a steep decrease in current after $\sim 60 \text{ s}$ of operation. The shorter *fs*PAG structures ($H \leq 200 \mu\text{m}$) showed less dynamic behavior but did exhibit a slow reduction of current during operation. Especially evident in the large structures, we attribute the initial current rise to an increase in gel temperature owing to Joule heating which, in turn, affects evaporation and ion concentration, leading to increased conductivity. In accordance, we attribute the observed subsequent sharp decrease in current to physical collapse of the gel structures owing to dehydration. Dehydration shrinks the porous gel matrix, thus reducing the conducting cross-section of the *fs*PAG lane. During the period when fluid is still present, the increasing resistance would reduce the current. Given these observations, we sought to minimize the rate of current drop to improve EMSA performance stability over an anticipated EMSA duration (Figure 3B). Using estimates from enclosed microchannel EMSAs of the *c*-di-GMP riboswitch (mobility shift of $2.5 \times 10^{-6} \text{ cm}^2/\text{V s}$, work in preparation), a 3 min separation is anticipated to allow full resolution of the mobility shift between bound and unbound riboswitch (Figure 3B). At this 3 min time point, a *fs*PAG structure with $H = 100 \mu\text{m}$ maintains $\sim 90\%$ of the initial current value, whereas the $H = 600 \mu\text{m}$ structure maintains just $\sim 40\%$ of the initial current. Consequently, all

subsequent EMSAs were conducted in *fs*PAG structures of 100 μm tall.

Glycerol Improves *fs*PAG Thermal, Structural, and Assay Performance. Glycerol offers a lower vapor pressure and evaporation rate than water,³³ thus we hypothesized that the addition of glycerol to the *fs*PAGE buffer should decrease the evaporative losses. However, the viscosity increase stemming from glycerol addition would also decrease analyte mobility and dispersion (via diffusion).^{34,35} While glycerol was employed as a sample additive in our previous *fs*PAGE protein assays, we sought here to understand the influence of glycerol contents on thermal and electrophoretic characteristics of the gel system as well as the assay repeatability during *fs*PAGE-EMSA in high conductivity buffers.²⁷ To determine a suitable glycerol concentration for *fs*PAG-EMSA, we investigated the *fs*PAGE by monitoring the electrical current, structural integrity, analyte mobility, analyte bandwidth, and resolving power of electrophoresis over a range of glycerol concentrations and electrophoresis times. In Figure 4A we monitored the electrical current in a 100 μm tall *fs*PAG every 10 s for a total 360 s of electrophoresis (60 V/cm). The *fs*PAGE run buffers contained varying glycerol concentrations from 0% to 30% (v/v). An immediate increase in relative current was observed during the first 30 s of electrophoresis followed by a monotonic decline in current over the remainder of the experiment. As expected, the additional glycerol concentration improved the electrical stability over the course of electrophoresis, as compared to systems with no glycerol present. Compared to a system with no glycerol, a system with 30% glycerol supported more than double the current after 6 min of operation (57.6% for 30% glycerol vs 23.5% for no glycerol). We attribute the improved current stability of a glycerol containing system to the enhanced *fs*PAG structural integrity resulting from reduced evaporative loss.

To explore the impact of glycerol addition on electrical conductivity, we measured both the current and the height of *fs*PAG structures after 0, 3, and 6 min of electrophoresis run times for a range of glycerol concentrations. Addition of glycerol to the run buffer increases hydrodynamic resistance^{34,35} and reduces ion mobilities. As detailed in Figure 4A, the initial current measured in a 30% glycerol device was 60% of the current measured in a *fs*PAG structure free of glycerol. We further noted that the addition of $>25\%$ glycerol to the *fs*PAG structures modulates electrical current stability over time (Figure 4A). Employing the *fs*PAG height as a proxy for the volume of solution retained in the *fs*PAG structure, we further observed that loss of *fs*PAG height during electrophoresis decreased with increasing glycerol concentration (Figure 4B). After 6 min of electrophoresis, the height reduction of *fs*PAG structures containing 30% glycerol was just $\sim 20\%$ lower than the initial structure height, whereas structures with no added glycerol saw height losses of $>80\%$. On the basis of these observations, we hypothesize that glycerol assists with maintaining *fs*PAG structural stability thus extending the effective electrophoresis time.

To evaluate the influence of enhanced viscosity (reducing mobility and diffusion) on the separation performance, we performed *fs*PAGE across a range of glycerol conditions on $H = 100 \mu\text{m}$ tall structures with fluorescent scalar TI*. For the conditions studied, the resultant TI* migration distance (L) and bandwidth (4σ) are reported in Figure 4C. As anticipated, increasing glycerol concentrations reduced both the TI* migration distance and bandwidth. To quantify the resolving

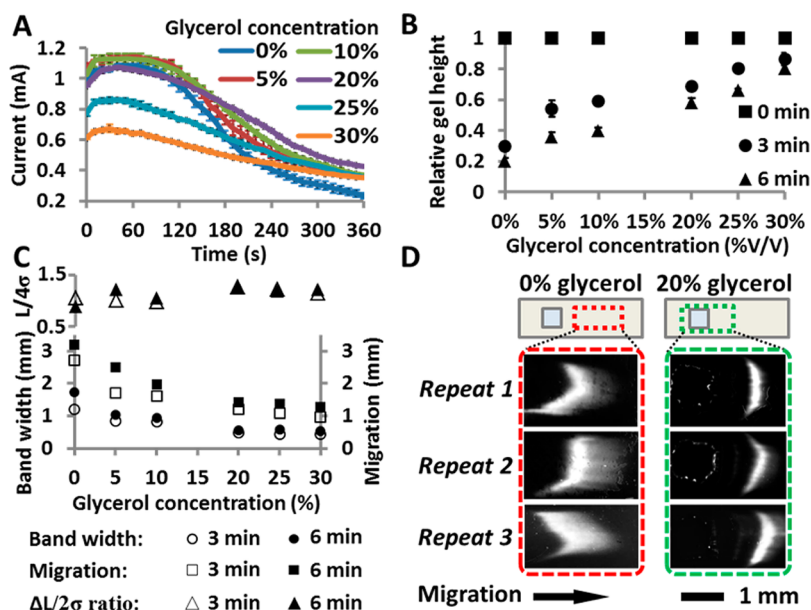


Figure 4. Glycerol addition improves *fsPAGE* operational stability. (A) Current dynamics of *fsPAG* structures with different glycerol concentrations. (B) Optical profilometry of gel height relative to initial structure height at set time points during *fsPAGE*. Initial height = 100 μm . (C) Measurements of migration distance, bandwidth, and their ratio at different glycerol concentrations during *fsPAGE* at 3 and 6 min. Protein: 500 nM OVA. (D) Fluorescence images of protein band migration during *fsPAGE* for 0% and 20% glycerol at 3 min during separation. $E = 60 \text{ V/cm}$. *fsPAG* height = 100 μm .

power, we considered the ratio between migration distance and bandwidth ($L/4\sigma$) as an approximation for separation resolution in more complex samples. After 3 and 6 min of electrophoresis time, structures containing glycerol yielded notably higher resolving powers than structures containing no glycerol.

To assess device reliability, we compared the band shape over three separate trials in structures with 0 and 20% glycerol concentrations. Figure 4D shows resultant images after 3 min of electrophoresis time, with dramatic band distortion and variation observed in the replicates with no glycerol present. Unsuitable repeatability and bad band shape control were likely caused by rapid evaporation, giving rise to nonuniform gel drying which leads to heterogeneity in analyte mobility across the gel. In contrast, structures containing higher glycerol concentrations (20%) yielded a consistent band with notably less transverse skew. Thus, run buffer containing 20% glycerol provided performance suitable for 3 to 6 min separations at (60 V/cm) in *fsPAG*-EMSA current stability, separation performance, and reliability.

Unit-to-Unit Variation Across a Large *fsPAGE* Array.

To realize a high-throughput EMSA platform, we fabricated a 96-plex 20% T 3.3% C *fsPAG* array measuring 60 mm \times 70 mm (Figure 5). The array is comprised of 8 parallel *fsPAG* lanes, each housing 12 separation units in series with a 4.5 mm unit-to-unit distance. To electrically address the array, graphite electrodes were placed atop electrode wicks orthogonal to each *fsPAG* lane and $\sim 2 \text{ mm}$ away from the first and last separation unit in each lane. In previous work, we observed significant unit-to-unit variation in analyte migration distance on large *fsPAG* arrays, especially in units on the periphery of the device.²⁷ To understand and address migration variation, we measured the migration distance of a scalar (fluorescently labeled 500 nM OVA*) at a set time and tested significance of unit-to-unit variation with an ANOVA test (Figure 5A and see the Supporting Information for details). In particular, we

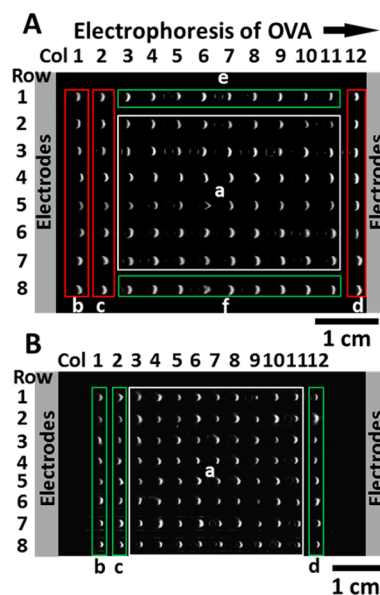


Figure 5. Unit-to-unit variation of migration distance on the 96-plex *fsPAGE*. (A) Fluorescence imaging of 96 concurrent OVA *fsPAGE*. A gel defect was detected in Row 5, Col 6, resulting in a “band bowing” on this unit (excluded from calculations). 96 units were grouped into regions. Central region group, a; other peripheral groups, b–f. F value for migration distance: a–b, 438; a–c, 121; a–d, 205; a–e, 0.14; a–f, 0.7. Significant variations were observed for a–b; a–c; and a–d (squared in red). No significant variations were observed for other groups (squared in green), $\alpha = 0.05$. (B) Optimized *fsPAGE* design with offset between electrodes and *fsPAG* units. Central region group, a; peripheral groups, b–d. F values: a–b, 1.67; a–c, 2.21; a–d, 0.05; no significant variations were observed (squared in green), $\alpha = 0.05$. $F_{\text{critical}} = 4.00$ for ANOVA on 96-plex *fsPAG*.

sought to assess the spatial variation in migration distance between peripheral groups and the central region (groups

assigned in Figure 5A). For each peripheral group, ANOVA was performed to analyze its variation against the central region group a, where no spatial variation is present. In the present ANOVA study with 96-plex *fs*PAGE, the F_{critical} value is 4.00 ($\alpha = 0.05$), meaning any calculated F value greater than 4.00 indicates significant difference in migration distance. For *fs*PAG lanes at the top and bottom of the array, no significant variation in migration distances were observed as compared to migration distances observed in the central array region (F values 0.14 and 0.70, respectively). In contrast, regions adjacent to the electrodes showed significant variation in scalar migration distance. As compared to the central region of the array, the first and second columns adjacent to the cathode electrode supported a higher scalar velocity (F values 438 and 121, respectively) and the 12th column directly adjacent to anode supported a lower scalar velocity (F value 205). We hypothesized that electrolysis during electrophoresis altered the pH proximal to each electrode. At the cathode, electrolysis should generate excess OH^- ions and elevate the local pH causing proteins to increases in negative charge and mobility. Conversely the anode would see generation of excess H^+ ions and lower the local pH, thus reducing protein charge and mobility.

While there were several possible approaches to address pH polarization, including increasing buffering capacity or implementing buffer reservoirs, we opted to simply redesign the electrode region of the 96-plex *fs*PAG array to offset the graphite electrodes from the first and last separation columns. The modified electrode regions increased the array area from 4200 mm^2 to 7000 mm^2 . With the offset electrode placement (Figure 5B), ANOVA reported no significant region to region variation in migration distance for the scalar ($F = 1.67, 2.21$, and 0.05 for columns 1, 2, and 12, respectively).

***fs*PAG-EMSAs for c-di-GMP Riboswitch on the 96-Plex *fs*PAG.** Having established the optimized *fs*PAG conditions, the 96-plex *fs*PAG-EMSAs were applied in high-throughput detection of binding of the Vc2 aptamer to c-di-GMP. On the basis of previous in-chip EMSAs as well as previously characterized Vc2 binding rates,³⁶ the expected interconversion rate between bound and unbound RNA is slower than the rate of electromigration, indicating that the EMSAs will resolve the binding-induced conformation change into two distinct bands. The separate bands visualized in the slow interconversion regime allow for the K_d or a standard curve of the system to be calculated by the relative intensity of each peak.³⁷

To analyze ligand binding to the Vc2 aptamer, we constructed a 96-plex 20% T 3.3% C *fs*PAG for high-throughput riboswitch *fs*PAG-EMSAs (Figure 6A). The array has 9 mm horizontal well-to-well spacing and 9 mm lane-to-lane distance such that a standard multichannel pipet provides a suitable macro-to-micro interface. The binding reactions contained 1 μM RNA and 0–900 nM c-di-GMP using 500 nM of TI* as an internal standard. On the basis of the high affinity of the Vc2 aptamer for c-di-GMP ($K_d \sim 11$ pM),³⁶ the high RNA concentration used here results in the generation of a standard curve rather than a K_d curve, which would require the concentration of one reagent to be below the K_d . Electrophoresis was performed for 2.5 min followed by fluorescence scanning of the array. The observed mobility shifts demonstrate the successful application of 96 parallel EMSAs in <3 min (Figure 6A). The ligand bound and unbound riboswitch were resolved within half the axial length of a unit, leaving room for further improvement in array density. Figure

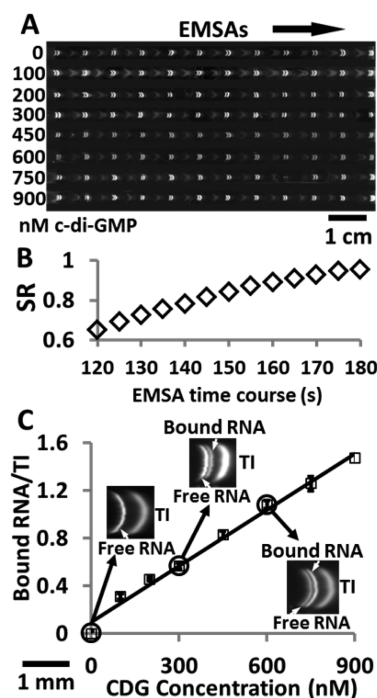


Figure 6. High-throughput *fs*PAG-EMSAs riboswitch. (A) Fluorescence images of c-di-GMP riboswitch EMSAs on a 96-plex *fs*PAG. Vc2 RNA (1 μM) was incubated with increasing concentrations of c-di-GMP (0–900 nM) and the binding reactions were assayed using TI* (500 nM) as the internal standard. The arrow points in the E -field direction. (B) SR monitoring showed mobility shift was resolvable at 2 min. (C) Normalized intensity of bound RNA increases with c-di-GMP concentration ($R^2 = 0.9893$). Insets zooms in the fluorescence micrographs of RNA separation.

6B reports the time evolution of the separation resolution between the unbound and the c-di-GMP-bound RNA, where the SR exceeds 0.5 from 2 min.

As shown in Figure 6C, the fluorescence intensity of the bound RNA band increases as the c-di-GMP concentration in the sample increases linearly ($R^2 = 0.9893$). Note that, for each concentration point, 12 repeats were averaged to improve the assay precision, yielding a standard error of less than 0.07 for all concentrations. The *fs*PAG-EMSA of 96 units in 10 min (5–6 min of setup and loading +3 min separation) yielded a throughput of ~ 10 data/min as compared to ~ 0.3 data/min¹⁷ for serially loaded, in-chip microfluidic EMSAs and ~ 0.01 data/min¹⁷ for slab PAGE-based EMSAs (17 h for 10 lanes).

CONCLUSION

To afford a capacity for concurrent operation of electrophoretic mobility shift assays, we explored *fs*PAG structures seated on an open planar polymer substrate. The open architecture allows for ready pipetting of a macroscale sample into microfluidic sample wells as well as compatibility with postseparation sample manipulation. To adapt the *fs*PAG for riboswitch EMSAs in high conductivity run buffers, we studied three major design aspects of the device, including (i) the dependence of EMSAs performance on sample well electrical properties (40%–100% loading of the sample well to maximize SR), (ii) the interplay between the *fs*PAG structure geometry and run buffer recipe, with the time dependent electrical properties of the system (100 μm *fs*PAG in 1 \times TBMK containing 20% glycerol yields the highest electrical stability), and (iii) the unit-

to-unit variation across the large-format fsPAG array and strategies for mitigation of variability (2 cm away from electrodes). Going forward we plan to further extend the fsPAG-EMSAs platform beyond its current capabilities. For instance, the present platform shows poor performance for electrophoresis times >3 min. For assays that require substantially longer separation times (>5 min), we are investigating a semienclosed fsPAG structure, which retains the facile open format while potentially providing longer separation duration. Additionally, the cumbersome manual loading process significantly limits the overall throughput of the assay (~5 min loading out of 10 min total assay). Automation of fsPAGE loading with robotic sample loading systems (<2 min loading) will likely further advance the screening capacity and impact of quantitative, precision EMSAs.

A pilot study of 96-plex fsPAG-EMSAs for the Vc2 c-di-GMP riboswitch aptamer binding reactions were demonstrated with linearity observed in a ligand concentration titration study. We envision that the improved detection sensitivity of the assay will allow K_d measurement for high-affinity interaction ($K_d < 1$ nM), and future studies will seek to harness the open gel structure to perform postseparation staining and signal amplification, further improving the detection sensitivity. Taken together, the streamlined yet powerful fsPAG-EMSAs offer a promising platform for rapid binding reaction analyses and support a molecular binding screening assay in a quantitative, high-throughput, and reliable manner.

■ ASSOCIATED CONTENT

Supporting Information

Additional information as noted in the text. This material is available free of charge via the Internet at <http://pubs.acs.org>.

■ AUTHOR INFORMATION

Corresponding Author

*E-mail: aeh@berkeley.edu.

Notes

The authors declare no competing financial interest.

■ ACKNOWLEDGMENTS

The authors acknowledge the Herr Lab members and Berkeley statistical consulting group for helpful discussion. This work was supported by NSF Graduate Research Fellowship (T.A.D.), Department of Defense NDSEG Fellowship (C.A.K.), NIH New Innovator Award (Grant No. 1DP2OD008677 to M.C.H.) and NSF CAREER Award (Grant CBET-1056035 to A.E.H.). M.C.H. holds a Career Award at the Scientific Interface from the Burroughs Wellcome Fund. A.E.H. is an Alfred P. Sloan Foundation Research Fellow in chemistry.

■ REFERENCES

- (1) Serganov, A.; Nudler, E. *Cell* **2013**, *152*, 17–24.
- (2) Mironov, A. S.; Gusarov, I.; Rafikov, R.; Lopez, L. E.; Shatalin, K.; Kreneva, R. A.; Perumov, D. A.; Nudler, E. *Cell* **2002**, *111*, 747–756.
- (3) Blount, K. F.; Breaker, R. R. *Nat. Biotechnol.* **2006**, *24*, 1558–1564.
- (4) Deigan, K. E.; Ferré-D'Amaré, A. R. *Acc. Chem. Res.* **2011**, *44*, 1329–1338.
- (5) Owicki, J. C. *J. Biomol. Screen* **2000**, *5*, 297–306.
- (6) Mere, L.; Bennett, T.; Coassin, P.; England, P.; Hamman, B.; Rink, T.; Zimmerman, S.; Negulescu, P. *Drug Discovery Today* **1999**, *4*, 363–369.
- (7) Yan, Y.; Marriott, G. *Curr. Opin. Chem. Biol.* **2003**, *7*, 635–640.
- (8) Choi, J. W.; Kang, D. K.; Park, H.; deMello, A. J.; Chang, S. I. *Anal. Chem.* **2012**, *84*, 3849–3854.
- (9) Srisa-Art, M.; Kang, D. K.; Hong, J.; Park, H.; Leatherbarrow, R. J.; Edel, J. B.; Chang, S. I.; deMello, A. J. *ChemBioChem* **2009**, *10*, 1605–1611.
- (10) Garner, M. M.; Revzin, A. *Nucleic Acids Res.* **1981**, *9*, 3047–3060.
- (11) Cann, J. R. *Anal. Biochem.* **1996**, *237*, 1–16.
- (12) Woodson, S. A.; Koculi, E. *Biophysical, Chemical, and Functional Probes of RNA Structure, Interactions and Folding, Part B; Methods in Enzymology*, Vol. 469; Elsevier: Amsterdam, The Netherlands, 2009; 469, pp 189–208.
- (13) Luo, Y. L.; Chen, B.; Zhou, J.; Sintim, H. O.; Dayie, T. K. *Mol. Biosyst.* **2014**, *10*, 384–390.
- (14) Mayer, G.; Raddatz, M. S. L.; Grunwald, J. D.; Famulok, M. *Angew. Chem., Int. Ed.* **2007**, *46*, 557–560.
- (15) Gomelsky, M. *Mol. Microbiol.* **2011**, *79*, 562–565.
- (16) Kulshina, N.; Baird, N. J.; Ferre-D'Amare, A. R. *Nat. Struct. Mol. Biol.* **2009**, *16*, 1212–1217.
- (17) Karns, K.; Vogan, J. M.; Qin, Q.; Hickey, S. F.; Wilson, S. C.; Hammond, M. C.; Herr, A. E. *J. Am. Chem. Soc.* **2013**, *135*, 3136–3143.
- (18) Stebbins, M. A.; Hoyt, A. M.; Sepaniak, M. J.; Hurlburt, B. K. *J. Chromatogr., B: Biomed. Appl.* **1996**, *683*, 77–84.
- (19) Ferrance, J.; Landers, J. P. *Luminescence* **2001**, *16*, 79–88.
- (20) Ross, D.; Kralj, J. G. *Anal. Chem.* **2008**, *80*, 9467–9474.
- (21) Emrich, C. A.; Tian, H. J.; Medintz, I. L.; Mathies, R. A. *Anal. Chem.* **2002**, *74*, 5076–5083.
- (22) Gaunt, T. R.; Hinks, L. J.; Rassoulalian, H.; Day, I. N. M. *Nucleic Acids Res.* **2003**, *31*, No. e48.
- (23) Gutzkow, K. B.; Langleite, T. M.; Meier, S.; Graupner, A.; Collins, A. R.; Brunborg, G. *Mutagenesis* **2013**, *28*, 333–340.
- (24) Wood, D. K.; Weingeist, D. M.; Bhatia, S. N.; Engelward, B. P. *Proc. Natl. Acad. Sci. U.S.A.* **2010**, *107*, 10008–10013.
- (25) Watson, C.; Ge, J.; Cohen, J.; Pyrgiotakis, G.; Engelward, B. R.; Demokritou, P. *ACS Nano* **2014**, *8*, 2118–2133.
- (26) Hughes, A. J.; Spelke, D. P.; Xu, Z.; Kang, C. C.; Schaffer, D. V.; Herr, A. E. *Nat. Methods.* **2014**, *11*, 749–755.
- (27) Duncombe, T. A.; Herr, A. E. *Lab Chip* **2013**, *13*, 2115–2123.
- (28) Wilson, S. C.; Cohen, D. T.; Wang, X. C.; Hammond, M. C. *RNA* **2014**, *20*, 1153–1160.
- (29) Duncombe, T. A.; Herr, A. E. *Anal. Chem.* **2012**, *84*, 8740–8747.
- (30) Herr, A. E.; Singh, A. K. *Anal. Chem.* **2004**, *76*, 4727–4733.
- (31) Hughes, A. J.; Lin, R. K.; Peehl, D. M.; Herr, A. E. *Proc. Natl. Acad. Sci. U.S.A.* **2012**, *109*, 5972–5977.
- (32) Stull, D. R. *Ind. Eng. Chem.* **1947**, *39*, 517–540.
- (33) Trevoy, D. J. *Ind. Eng. Chem.* **1953**, *45*, 2366–2369.
- (34) Pennings, S.; Meersseman, G.; Bradbury, E. M. *Nucleic Acids Res.* **1992**, *20*, 6667–6672.
- (35) Hu, C. T.; O'Shaughnessy, K. M. *Electrophoresis* **2001**, *22*, 1063–1068.
- (36) Smith, K. D.; Lipchock, S. V.; Ames, T. D.; Wang, J.; Breaker, R. R.; Strobel, S. A. *Nat. Struct. Mol. Biol.* **2009**, *16*, 1218–1223.
- (37) Pan, Y.; Karns, K.; Herr, A. E. *Electrophoresis* **2014**, *35*, 2078–2090.